

# Accepted manuscript doi: 10.1680/jgeot.21.00090

---

## **Accepted manuscript**

As a service to our authors and readers, we are putting peer-reviewed accepted manuscripts (AM) online, in the Ahead of Print section of each journal web page, shortly after acceptance.

## **Disclaimer**

The AM is yet to be copyedited and formatted in journal house style but can still be read and referenced by quoting its unique reference number, the digital object identifier (DOI). Once the AM has been typeset, an 'uncorrected proof' PDF will replace the 'accepted manuscript' PDF. These formatted articles may still be corrected by the authors. During the Production process, errors may be discovered which could affect the content, and all legal disclaimers that apply to the journal relate to these versions also.

## **Version of record**

The final edited article will be published in PDF and HTML and will contain all author corrections and is considered the version of record. Authors wishing to reference an article published Ahead of Print should quote its DOI. When an issue becomes available, queuing Ahead of Print articles will move to that issue's Table of Contents. When the article is published in a journal issue, the full reference should be cited in addition to the DOI.

**Submitted:** 05 May 2021

**Published online in ‘accepted manuscript’ format:** 14 July 2022

**Manuscript title:** Undrained uplift resistance of under-reamed open caisson shafts

**Authors:** Brian B. Sheil\*, Jack O. Templeman\*, Zhandos Orazalin\*, Bryn M. Phillips\*,<sup>†</sup> and Geyang Song\*

**Affiliations:** \*Department of Engineering Science, University of Oxford, Oxford, UK and

<sup>†</sup>Ward and Burke Construction Ltd, Unit N, Bourne End Business Park, Bucks, UK

**Corresponding author:** Brian B. Sheil, Department of Engineering Science, University of Oxford, Parks Road, Oxford, OX 3PJ, UK.

**E-mail:** brian.sheil@eng.ox.ac.uk

## **Abstract**

Deep large-diameter caisson shafts are a popular means of constructing underground storage and attenuation tanks and pumping stations for the water and wastewater industry. One of the key design concerns for these structures is resistance to flotation during periods where the tanks are only partially filled or empty. This paper uses two-dimensional numerical analysis to explore the undrained uplift resistance provided by under-reaming the walls of the caisson shaft to create an enlarged base. The primary aim of the study is to assess the influence of the taper angle of the anchor (i.e. the protruded base) on the resulting uplift resistance. The effects of the anchor-soil interface roughness factor, soil weight, surcharge pressure, and caisson radius are also investigated. The results indicate that the effect of the taper angle on both the uplift bearing capacity and the developed horizontal reaction can be very significant. The numerical output informs the development of a closed-form approach for application in routine design. The new design method is shown to provide an excellent agreement with both finite element and additional finite element limit analysis calculations. By way of example, the proposed design method is applied to a hypothetical design scenario.

**Keywords:** bearing capacity; caissons; clays; finite-element analysis

## INTRODUCTION

Deep large-diameter caisson shafts are popular as underground storage, attenuation tanks, and pumping stations for the water and wastewater industry (see Fig. 1; Phillips et al. 2019; Royston et al. 2020a; Templeman et al. 2021). Given their large depth and internal volume, groundwater-induced uplift pressures acting on the caisson base can be significant. For this reason, a key design concern for these structures in the permanent state is flotation when the tanks are emptied due to the significant reduction in downward force. For monolithic caissons, the use of lubricating fluids to minimise external caisson-soil friction during the sinking process (Sheil & Templeman 2022) means that long-term anti-flotation frictional resistance is typically neglected in design.

This leaves three design options for anti-flotation: (a) reacting off tank projections such as adjoining tunnels, (b) under-reaming the walls of the shaft post-sinking to create an enlarged base, and (c) increasing the dead weight of the shaft base and walls. Typically, adjoining structures are insufficient to resist flotation. The lack of research into the uplift resistance provided by an enlarged base for this problem means that option (c) is typically adopted in the industry. This is achieved by excavating the structure deeper and casting an excessively thick base at great economic and environmental expense. Therefore, there is significant motivation to develop rigorous solutions for the anti-flotation resistance contribution of an enlarged caisson base (option (b)).

Anti-flotation of an enlarged caisson base is analogous to the uplift response of annular plate anchors. Embedded plate anchors are one of the most common anchoring systems due to their low cost and straightforward installation. The uplift capacity of a plate anchor is typically expressed in terms of an uplift factor which is a function of the anchor shape, soil properties, embedded depth, and overburden pressure. In addition, there exists a critical embedment depth at which the failure mechanism no longer extends to the soil surface and becomes fully localised around the anchor.

Vesic (1971) documented one of the earliest studies into the behaviour of plate anchors subjected to uplift loading, proposing theoretical solutions for the uplift capacity for strip and circular plate anchors embedded in both sand and clay. Informed by model-scale laboratory testing, Das (1978, 1980) and Das et al. (1985a,b,1994) reported modifications to the uplift bearing capacity factors to account for strip, square, rectangular, and circular plate anchors in clay. For anchors embedded in fine-grained soils, a key contribution to the anchor pull-out resistance is suction development at the anchor-soil interface. Using finite element analysis (FEA) techniques, many investigators have sought to quantify the magnitude of this contribution and its dependence on the anchor loading rate e.g. Rowe and Davis (1982), Thorne et al. (2004), Song et al. (2008), Wang et al. (2010). More recently, Jesmani et al. (2013) and Zhao et al. (2015) explored the role of the anchor inclination angle on the vertical uplift capacity. Arguably the greatest contribution to our understanding of plate anchor capacity and associated failure mechanisms has been achieved through the application of upper- and

lower-bound plasticity theory. This has included the role of anchor inclination and shape (Merifield et al. 2001, 2003, 2005; Merifield and Sloan 2006; Bhattacharya and Kumar 2014; Yu et al. 2015), soil strength profile (e.g. Yu et al. 2015), load inclination and eccentricity (e.g. Kumar and Rahaman 2018), and scale effects in sands (e.g. Roy and Bhattacharya 2018).

While the requirements for plate anchors to resist various forms of loading and at a range of depths have been well covered in the literature, their application to anti-flotation resistance of open caissons is unique; further research is therefore warranted for reliable application in practice. To address this shortcoming, this paper uses three different two-dimensional numerical techniques to explore the undrained uplift resistance of an under-reamed open caisson shaft. Conventional small-strain FEA is used to assess the influence of the anchor taper angle and interface roughness factor, the soil weight, and the caisson radius on the resulting uplift resistance and developed horizontal reaction. The results are validated using rigorous finite element limit analyses. Finally, a limited number of large deformation FEA calculations are performed to explore the role of large soil deformation effects. The numerical output informs the development of a closed-form approach for application in routine design which is applied to a hypothetical design scenario.

## PROBLEM DEFINITION

Figure 2 describes the problem considered in this study. A shaft with an enlarged under-reamed base, resembling a tapered plate anchor of width  $b$  and taper angle  $\beta$ , is considered embedded in undrained Tresca soil. The soil has a shear strength profile defined as  $s_u(z) = s_u - kz$  and unit weight,  $\gamma_s$  where  $s_u$  is always the undrained shear strength at the anchor apex,  $k$  is the increment of strength with depth and  $z$  is the elevation relative to the anchor apex as shown in Fig. 2. This work focuses on deep shafts such that the problem reduces to deep-seated localised failure (Royston et al. 2016, 2020b). The strength of the anchor-soil interface is defined as  $\alpha s_u$  where  $\alpha$  is the interface roughness factor, which can vary between 0 ('smooth') and 1 ('rough'). The shaft is translated vertically upwards with velocity  $v_0$  by a vertical load  $V$ , which may also induce a horizontal reaction,  $H$ , for an inclined anchor. The interface between the vertical shaft wall and surrounding soil is assumed smooth based on empirical evidence for the effectiveness of an external annulus and interface lubrication during caisson sinking in undrained soils (Royston, 2018; Royston et al., 2020b; Sheil 2021). Whilst it is possible for the soil to regain contact with the exterior caisson surface or for the interface to be grouted in the permanent state (and therefore develop friction), the frictional resistance contribution for anti-uplift is widely ignored in design; this simplification, therefore, ensures any resulting bias is on the conservative side for this problem.

No-tension conditions were imposed at the interface between the shaft base and the soil to avoid unconservative reliance on the suction resistance contribution. The results of the modelling are presented in terms of a dimensionless uplift factor  $N_p = V/s_u b$  for plane strain (PS) conditions ( $R_0 = \infty$  where  $R_0$  is the external radius of the shaft; see Fig. 2) where  $V$  is expressed as the uplift force per unit length. Axisymmetric conditions are characterised by the dimensionless caisson radius  $b/R_0$ , and the dimensionless uplift factor is expressed as  $N_{axi} = V/s_u A$ , where  $V$  is now defined as the total uplift force and  $A$  is the plan cross-sectional area of the anchor.

## FINITE ELEMENT ANALYSES

### *Finite element model*

The FEA calculations were performed using the software package Abaqus/Standard (Dassault Systèmes, 2017). The soil was modelled using 6-node quadratic, hybrid triangular elements (CPE6H and CAX6H for plane strain and axisymmetric conditions, respectively). The anchor was modelled using a separate body meshed with 2-node rigid elements (R2D2) tied to a reference node to create a rigid body. The interaction between the soil and anchor was modelled using a surface-to-surface contact with finite-sliding formulation and a rigid-plastic material with a shear strength of  $\alpha s_u$ . Horizontal displacements were prevented at the lateral boundaries of the soil domain, whereas the bottom boundary was fully fixed. The top boundary was also restricted from movement normal to the top surface to mimic the behaviour of a deep shaft.

### *Material model*

The constitutive model adopted in this study was an isotropic, linear elastic model with perfect plasticity, governed by a rounded approximation to the Tresca yield criterion. The criterion presented by Abbo et al. (2011) was used, as shown in Fig. 3, which uses trigonometric rounding in the octahedral plane to smooth the yield criterion in the vicinity of the edge discontinuities (Fig. 3). The approximation is governed by the Lode angle at which transition to the rounded approximation occurs,  $\theta_T$ ; away from the discontinuities (i.e.  $|\theta| < \theta_T$ ), the approximation matches the conventional Tresca criterion exactly. Typical values for  $\theta_T$  are in the range of  $25^\circ$  to  $29.5^\circ$  (Abbo et al., 2011). In this study, a transition angle of  $\theta_T = 29^\circ$  was adopted. This gives a conservative approximation that closely models the conventional Tresca criterion and is continuous in both its gradient and gradient derivative at all stress states thereby providing a robust numerical implementation.

The soil material model was implemented in Abaqus/Standard using a user-defined material subroutine (UMAT) written in Fortran. The adopted integration technique is based on the explicit modified Euler numerical stress integration scheme, with adaptive sub-stepping and error control, presented by Sloan et al. (2001). The present approach uses the algorithms proposed by Sloan et al. (2001) to identify the yield surface intersection during elastic-to-plastic transitions and to handle

elastoplastic transitions. Stress correction is also performed to return the updated stresses to the yield surface after each substep, if the yield tolerance is exceeded. In this study, the tolerances on the yield function evaluation and stress error (FTOL and STOL respectively in Sloan et al. (2001)) were both taken to be  $1 \times 10^{-6}$ .

#### *Adaptive remeshing*

To obtain accurate uplift factor predictions, an adaptive mesh refinement procedure was adopted, as described in Martin (2011) and summarised in Fig. 4. The initial analysis starts with the creation of a planar straight-line graph (PSLG) representing the user-defined geometry of the problem. The open-source program Triangle (Shewchuk, 1996, 2002) is used to generate an initial 2D unstructured triangular mesh of the PSLG using conforming constrained Delaunay triangulation. These mesh details are automatically extracted and incorporated into an Abaqus FEA input file using Matlab programming. The modelling procedure then enters a series of remeshing iterations, in which the soil domain mesh is progressively refined based on the previous FEA results. Note the remeshing process occurs after a complete standalone analysis of the problem rather than *during* an integrated analysis. The initial iterations are performed on very coarse meshes and the process quickly converges such that only the final calculation is performed on a detailed optimised mesh. The adopted framework therefore avoids the need to map state parameters between meshes and for expensive heuristic boundary and mesh sensitivity studies. In this work, the remeshing scheme seeks to equalise the integral of the maximum shear strain rate over all elements in the mesh. In each iteration, Triangle is called to refine the previous analysis mesh based on calculated target area values before a new FEA input file is generated and supplied to Abaqus.

#### *Finite element calculation stages*

The following stages of analysis were adopted to model the problem defined by Fig. 2:

- I. Initialisation of soil stresses through the application of a body force to the soil domain in the vertical direction within a geostatic step for stress equilibration. Horizontal stresses are determined from the user-defined input of the coefficient of lateral earth pressure,  $K_0 = 1$ .
- II. Wished-in-place installation of a weightless, rigid anchor of the width  $b = 1$  m and taper angle  $\beta$  in undrained soil with the shear strength  $s_u = 1$  kPa and undrained Poisson's ratio  $\nu_u = 0.495$ . An unrealistically large value of  $E_u/s_u = 25,000$  was chosen to approximate rigid-plastic soil behaviour where  $E_u$  is the undrained Young's modulus of the soil. The pre-defined anchor-soil interaction behaviour was also activated in this step where no tension interface conditions were imposed at the base of the anchor to prevent suction development. The anchor was restrained in all three degrees of freedom during this calculation phase.

- III. Application of an upward prescribed displacement,  $u$ , until failure is achieved, defined by a plateau in the load-displacement curve. During this step, the shaft was constrained to move only vertically (no lateral movement or rotation).

#### *Large deformation analyses*

For low values of  $E_u/s_u$ , large vertical displacements may be required to induce the flow-around failure mechanism. This is likely to cause numerical convergence issues with conventional FEA, particularly if a very fine mesh is used, due to excessive deformation of the mesh elements. To explore the influence of soil stiffness, a small number of analyses were performed using large deformation FEA (LDFEA). Whilst many options exist (e.g. the arbitrary Lagrangian-Eulerian technique, the coupled Eulerian-Lagrangian method), the RITSS (remeshing and interpolation technique with small strain) approach was used here (Hu & Randolph, 1998). This method was selected as it can be applied to the same model configuration used for the present small-strain FEA.

In RITSS, a large displacement is applied through a series of smaller increments, which are each handled by conventional small-strain FEA linked together using Python programming. After each completed analysis, the deformed geometry is extracted and remeshed to form the subsequent analysis. The values of any field/solution variables at the end of the prior analysis are mapped/interpolated to the new mesh, to form initial conditions for the subsequent analysis. Equilibrium of the mapped state is then obtained before the next incremental displacement is applied. This process is repeated to achieve the full large displacement required. The issue of mesh deformation is overcome by reforming the mesh topology for each analysis manually within the Abaqus environment and by ensuring each incremental analysis is sufficiently small. Non-linear (NL) geometric effects are considered using the 'NLgeom' feature in Abaqus.

#### **FINITE ELEMENT LIMIT ANALYSES**

A limited number of analyses were completed using finite element limit analysis (FELA) to provide further validation of the present study. These analyses made use of the package Optum G2 (Krabbenhoft et al. 2016). The soil was modelled as a rigid-plastic Tresca material while the anchor was modelled as a rigid body. For each problem, an analysis was conducted using strict lower- (LB) and upper-bound (UB) plasticity solutions. The LB analyses used triangular elements with a linear variation in stresses between corner nodes such that yield conditions are enforced at the three corner nodes. The UB analyses used triangular elements with quadratic interpolation of displacements and linear interpolation of stresses within each element. This process allows a rigorous bracketing of the exact collapse loads where the difference between UB and LB was typically <1% such that the final collapse loads were obtained by averaging the final LB and UB collapse multipliers. Each model was initially uniformly discretised with 1,000 elements. The total number of elements at the end of the



analysis varied up to a maximum of 10,000 elements after seven rounds of adaptive meshing, based on the distribution of plastic shear dissipation.

## VALIDATION OF NUMERICAL METHODS

To validate the developed finite element methodology, a conventional deeply embedded horizontal ( $\beta = 0^\circ$ ) plate anchor was analysed, and the resulting uplift capacity was compared to existing solutions for weightless soil with uniform strength (see Table 1). The FEA calculated value of  $N_p$  was determined as 11.459 and 11.457 for a smooth and rough interface, respectively, and 11.454, 11.461 and 11.464 for intermediate roughness values of  $\alpha = 0.25, 0.5$  and  $0.75$ , respectively. These values correspond very well with the present FELA results as well as the results documented by Merifield et al. (2001) and O'Neill et al. (2003).

Figure 5 shows an exemplar FEA mesh before and after five iterations of the custom refinement procedure described by Fig. 4. The elements become increasingly refined from the initial coarse mesh (Fig. 5(a)) in regions where the intensity of maximum principal strain rate is greatest. This results in velocity discontinuities appearing as dark bands of high concentration of small elements (Fig. 5(b)); regions of diffuse plastic shearing undergo intermediate levels of refinement, and rigid blocks remain largely unrefined (Martin, 2011).

## FEA RESULTS: UPLIFT RESISTANCE

### *Inclined plane strain anchors*

FEA analyses were performed to explore the influence of both the taper angle,  $\beta$ , and anchor interface roughness factor,  $\alpha$  on the ultimate uplift resistance, as well as the associated soil failure mechanisms. Figure 6 shows the refined finite element meshes superimposed on the soil displacement field at failure for salient values of  $\alpha$  (0, 0.5 and 1) and  $\beta$  ( $30^\circ$ ,  $45^\circ$  and  $60^\circ$ ). Corresponding FEA-calculated values of  $N_p$  are also given with each figure.

In all cases, soil failure corresponds to a local ‘flow-around’ mechanism comprising a rigid triangular region beneath the anchor, a shear fan zone and (for  $\beta < 45^\circ$ ) another rigid triangular region immediately above the anchor. While there is a vertical component to the displacement of the rigid triangular wedge beneath the anchor, this occurs at a different rate to the caisson movement such that breakaway occurs at the interface. The refined mesh reveals that no plastic shear deformation occurs between the triangular wedge above the anchor and the shear fan zone except for  $\alpha = 1$  and  $\beta = 30^\circ$ . Furthermore, no plastic shear deformation occurs between the triangular wedge beneath the anchor and the shear fan zone in all cases. The interior angles of the upper rigid triangle are controlled by  $\alpha$ , which in turn influences the size of the failure mechanism. It can also be seen that  $\beta$  influences the uplift resistance by two competing mechanisms. Firstly, an increase in  $\beta$  increases the anchor length for a given value of  $b$ , thereby, increasing resistance. However, this is offset by a reduction in the

subtended angle of the shear fan zone angle as the interior angles of the rigid region above the anchor remain unchanged. By way of example, for  $\alpha = 0$ , an increase in  $\beta$  from  $30^\circ$  to  $60^\circ$  causes a 10% reduction in  $N_p$  whereas a 2% increase can be observed for  $\alpha = 1$ . It is worth remarking that for  $\alpha = 1$  and  $\beta \leq 45^\circ$ , the value of  $N_p$  is the same as that obtained for a conventional deeply buried horizontal plate anchor.

Figure 7 plots the FEA-calculated influence of  $\beta$  on  $N_p$ . For a rough anchor,  $N_p$  is independent of the taper angle for  $\beta \leq 45^\circ$ , as shown in Fig. 7(a). This is due to the rigid wedge above the anchor which forms an angle of  $45^\circ$  to the horizontal for  $\alpha = 1$  (see Fig. 6). However, for  $\beta > 45^\circ$ , the value of  $N_p$  begins to increase. A reduction in  $\alpha$  has three main influences on the relationship between  $N_p$  and  $\beta$ : (a) the range for which  $N_p$  is independent of  $\beta$  is reduced, (b) the relationship between  $\beta$  and  $N_p$  becomes linear, and (c) an increase in  $\beta$  causes a reduction in  $N_p$ . The influence of  $\gamma_s b/s_u$  on the relationship between  $\beta$  and  $N_p$  is explored in Fig. 7(b). An increase in the soil unit weight causes a reduction in the uplift capacity due to additional buoyant uplift forces. This reduction is of course independent of  $\alpha$  but increases with  $\beta$  as the buoyant uplift force is dependent on the area occupied by the anchor.

#### *Inclined axisymmetric anchors*

Figure 8 shows the influence of the dimensionless caisson radius,  $b/R_0$ , on the soil failure mechanisms using refined finite element meshes superimposed on the soil displacements at failure for extremum taper angles of  $\beta = 0^\circ$  and  $75^\circ$ . Corresponding FEA-calculated values of  $N_{axi}$  are also superimposed on each figure. A reduction in the caisson radius influences the soil failure mechanism as follows: (a) the shape of the shear fan zone transitions from circular to spiral, (b) plastic work occurs in the now deforming wedge, and (c) the circumferential length of the failure surface reduces leading to an increase in the shear strain. These factors combine to produce notably greater uplift capacity factors.

Figure 9 plots the development of  $N_{axi}$  with an increase in  $b/R_0$ , normalised by the equivalent PS value ( $N_p$ ), for a range of  $\beta$  and for both smooth and rough anchor interface conditions. From Fig. 9(a), the relationship between  $b/R_0$  and  $N_{axi}/N_p$  is both non-linear and highly dependent on the anchor taper angle: for  $\beta = 75^\circ$ , the capacity of an anchor with  $b/R_0 = 0.3$  is 13% greater than the equivalent PS value compared to only 3% greater for  $\beta = 0^\circ$ . In contrast, comparing Figs. 9(a) and 9(b) reveals that while  $\alpha$  also has an effect, its influence relative to both  $\beta$  and  $b/R_0$  is secondary. For large values of  $\beta$ ,  $b/R_0$  has the greater influence on the capacity if the interface is smooth and vice versa for low values of  $\beta$ .

---

*Influence of soil strength profile*

The influence of the soil strength gradient,  $k$ , non-dimensionalised as  $kb/s_u$ , is explored for both PS and axisymmetric conditions in Figs. 10(a) and 10(b) respectively. In this case,  $s_u$  is taken as the undrained shear strength at the apex of the anchor for the determination of  $N_p$  and  $N_{axi}$ . Figure 10 shows that values of  $N_p$  and  $N_{axi}$  for  $\alpha = 0$  are identical for both strength profiles. When the anchor roughness is increased to  $\alpha = 1$ , there is a slight difference in  $N_p$  and  $N_{axi}$  for the largest value of  $\beta$ : 4.7% and 6.0% respectively. Nevertheless, these results show that the value of  $s_u$  at the anchor apex represents a very good approximation for the average  $s_u$  integrated over the soil failure mechanism. Therefore, the present work can be considered applicable to any soil profile whose strength varies linearly with depth.

*Influence of soil stiffness*

The influence of soil stiffness on the development of  $N_p$  with dimensionless uplift displacement ( $u/b$ ) for a PS anchor is presented in Fig. 11. LDFEA calculations for values of  $E_u/s_u$  of 2000, 5000 and 10000 considering both linear (L) and non-linear geometric effects are compared with the value obtained using conventional small-strain FEA. There is excellent agreement between the FEA and LDFEA calculations (considering linear geometric effects only) revealing an insignificant influence of the changing geometry of the problem during uplift. When NL geometric effects are considered, LDFEA provides notably larger calculations of the uplift capacity factor after the initial onset of yield followed by post-peak softening. This effect is highly dependent on the value of  $E/s_u$  such that additional capacity benefits arising from large soil deformation effects may not necessarily be reliable in design. While these results reveal an important role of large soil deformation effects, it can be concluded that the small-strain calculation provides an expedient calculation with a bias on the safe side for this problem.

**FEA RESULTS: DEVELOPED HORIZONTAL REACTION**

Due to the inclination of the anchor, the development of significant horizontal reactions during vertical uplift is feasible, which may also be of interest from a structural design perspective. To this end, Fig. 12 plots the normalised horizontal reaction,  $\hat{H}_p = H/s_u b$ , as a function of the taper angle where the subscript 'p' denotes PS conditions and  $H$  is the horizontal force per unit length. The results show that the use of a steep taper angle (high  $\beta$ ) has the potential to induce a large horizontal reaction on the anchor and, therefore, significant compressive stresses in the walls at the base of the shaft. It is also noteworthy that the relationship between  $\hat{H}_p$  and  $\beta$  appears independent of  $\alpha$ ; this is because the horizontal reaction is dominated by the normal stress contribution of the soil strength and unit weight. The influence of the dimensionless caisson radius on these results is explored in Fig. 13 where  $\hat{H}_{axi}$  is the normalised horizontal reaction for the axisymmetric case i.e.  $\hat{H}_{axi} = H/s_u A$ . Extension of the

problem to axisymmetric behaviour now introduces a sensitivity to  $\alpha$ . Except for the  $\beta = 15^\circ$  case, an increase in  $\alpha$  from 0 to 1 causes a notable increase in the developed horizontal reaction. It is also worth remarking that the trends for  $\alpha = 0$  presented in this figure are identical to the corresponding results for  $N_{\text{axi}}/N_p$  presented in Fig. 9(a) due to the absence of the shear resistance contribution. The influence of soil stiffness on the development of  $\hat{H}_p$  with dimensionless uplift displacement ( $u/b$ ) for a PS anchor is presented in Fig. 14. LDFA calculations for values of  $E/s_u$  of 2000, 5000 and 10000 are again compared with the conventional small-strain FEA value. There is excellent agreement between the LDFA (L) and FEA small-strain calculations of the horizontal reaction. Consideration of large soil deformation effects reveals a significant influence on the peak horizontal reaction, particularly for large values of  $E/s_u$ . Therefore, it is prudent to incorporate large soil deformation effects in situations where the developed horizontal is a realistic design concern.

## DESIGN METHOD DEVELOPMENT

### *Uplift resistance of plane strain anchors*

While direct numerical analyses of geotechnical problems are becoming more commonplace, simplified design approaches remain an integral part of preliminary design. This is particularly the case for the design of large-diameter open caissons, where the selection of various construction details typically rests with the contractor. Therefore, the FEA results presented in this paper were used to inform the development of closed-form equations suitable for use in routine design.

Complexity is added to the analysis of the uplift capacity in two stages: (i) PS and (ii) axisymmetric conditions. Based on the FEA calculated soil failure mechanisms (Fig. 6), two mechanisms are proposed for the determination of the ultimate uplift load using an upper bound (UB) plasticity analysis (see Fig. 15). Mechanism I (Fig. 15(a)) consists of a rigid body ABCA which moves vertically upwards with the anchor. This mechanism is only valid for  $\beta \leq 45^\circ$ . No shear takes place at the anchor-soil interface AB and BC and there exists a shear fan zone ACDA about point A. Finally, there is a rigid region ADEA that translates parallel to the side ED.

This geometry is defined by the following angles:

$$\theta_I = \frac{\pi}{4} - \beta \quad (1)$$

$$\theta_{II} = \frac{3\pi}{2} \quad (2)$$

$$\theta_{III} = \frac{\pi}{4} \quad (3)$$

The lengths of the associated velocity discontinuities are presented in Table 2. The ultimate load  $V$  is determined by equating the work done by the external forces  $\Delta W_p$  and soil weight  $\Delta W_s$  to the energy dissipated by the internal soil stresses  $\Delta E$ . The work done by the external forces can be defined as:

$$\Delta W_p = v_o V \quad (4)$$

The energy dissipated by the internal stresses is equal to the sum of (a) the work done along each velocity discontinuity, which is a function of the velocity jump at the discontinuity, and (b) the work done within the plastically deforming region ACDA, which is a function of the velocity. The velocity jumps along discontinuities AC ( $\Delta v_{AC}$ ), CD ( $\Delta v_{CD}$ ) and DE ( $\Delta v_{DE}$ ), and the velocities within region ACDA ( $v_{s,CD}$ ) can be obtained from the geometry of Fig. 15(a) and are presented in Table 2. Also presented in the same table are the work calculations for the internal stress mechanism, which sum to give  $\Delta E$ :

$$\Delta E = s_u v_0 b (2 + 3\pi) \quad (5)$$

Equating the external work done with the internal energy dissipation, the ultimate uplift capacity can be expressed in dimensionless form as follows:

$$N_p = 2 + 3\pi \quad (6)$$

The key difference between mechanism II and mechanism I in the existence of a velocity discontinuity at the anchor-soil interface AB, which introduces a dependence on  $\alpha$ , and the presence of an additional rigid wedge ABCA that moves perpendicular to AC (see Fig. 15(b)). The geometry can be defined using one optimisation parameter ( $\theta_I$ ). Angle  $\theta_{III} = \pi/4$  and  $\theta_{II}$  can be expressed in terms of  $\theta_I$  as follows:

$$\theta_{II} = \frac{7\pi}{4} - \beta_{rad} - \theta_I \quad (7)$$

Where  $\beta_{rad}$  is the taper angle expressed explicitly in radians. The lengths of the associated velocity discontinuities are presented in Table 3. The velocity jumps along the relevant discontinuities, and the velocities within region ACDA ( $v_{s,CD}$ ) are obtained from the geometry of Fig. 15(b), and are also presented in Table 3. Equating the external work done and the energy dissipated by the internal soil stresses, the dimensionless uplift capacity factor can be defined as follows:

$$N_p = \frac{1}{\sin(\frac{\pi}{2} + \theta_I)} \left[ \alpha \sin(\beta_{rad} + \theta_I) + \sin\left(\frac{\pi}{2} - \beta_{rad}\right) \left( \sin(\theta_I) + 2 \cos(\theta_I) \left( \frac{7\pi}{4} - \beta_{rad} - \theta_I + 0.5 \right) \right) \right] \quad (8)$$

In Fig. 16, the optimised upper bound mechanisms for  $\beta = 45^\circ$  and  $\alpha$  ranging between 0 and 1 are compared to the incremental shear strains at failure determined using FEA. It is worth noting that the optimised upper bound provides the exact solution for plane strain conditions and is in excellent agreement with the FEA failure mechanisms.

Due to asymmetry about the vertical axis of the cutting face, the influence of soil unit weight on the uplift resistance necessitates explicit treatment. The work done by the soil unit weight,  $\gamma_s$ , is defined as follows:

$$\Delta W_s = \frac{1}{2} v_0 \gamma_s b^2 \tan \beta \quad (9)$$

The negative resistance contribution attributed to soil unit weight is therefore captured by the second term on the right-hand side of equation (10) and is a function of  $\beta$ :

$$V_p = \left( N_p s_u - \frac{1}{2} \gamma_s b \tan \beta \right) b \quad (10)$$

Where  $V_p$  is the uplift resistance for a plane strain anchor. Predictions of the uplift capacity factor determined using the proposed UB approach, defined by equations (6) and (8), are presented in Table 4 for values of  $\alpha$  ranging between 0 and 1 and salient values of  $\beta$ . It can be seen that mechanism I dominates for low values of  $\beta$  and high values of  $\alpha$  and vice versa for mechanism II. The UB calculations are in excellent agreement with those determined using FEA and FELA, where the maximum deviation is 0.6%.

#### *Uplift resistance of axisymmetric anchors*

For non-planar problems, it is often challenging to construct a high-fidelity velocity field that is both kinematically admissible and easily calculable. The design method for PS anchors was therefore extended to axisymmetric conditions by direct curve-fitting of the FEA output. It was found empirically that the development of  $N_{axi}/N_p$  is a linear response to an increase in  $b/R_0^{0.7}$ ; the following expression was therefore used to extend equations (6) and (8) to axisymmetric conditions:

$$N_{axi} = N_p \left( 1 + m \left( \frac{b}{R_0} \right)^{0.7} \right) \quad (11)$$

Where the curve-fitting parameter  $m$  represents the gradient of the  $N_{axi}/N_p - b/R_0^{0.7}$  relationship. An expression for  $m$  was developed by fitting a linear relationship to the FEA data and further regressing the fitted slope on the parameters  $\alpha$  and  $\beta$ . This exercise yielded the following expression:

$$m = (0.05 - 0.035\alpha) \tan((1.04 + 0.07\alpha)\beta_{rad}) + 0.066 + 0.047\alpha \quad (12)$$

The resulting axisymmetric vertical uplift resistance,  $V_{axi}$ , is determined using equation (13), where the volume of a truncated hollow cone is used for the calculation of the soil buoyancy term:

$$V_{axi} = \left( N_{axi} s_u A - \gamma_s \pi \tan \beta \left[ b^2 R_0 + \frac{b^3}{3} \right] \right) \quad (13)$$

Equation (11) was used to re-predict the anchor uplift factor for all analyses considered in the preceding parametric study; the results are compared to the FEA and FELA output in Fig. 17 where excellent agreement can be observed.

#### *Developed horizontal reaction*

The kinematic failure mechanisms shown in Fig. 15(a) inform the development of a theoretical expression for the horizontal reaction for plane strain conditions:

$$H_p = \frac{b}{\cos(\frac{\pi}{4})} \left[ \left( s_u (1 + 3\pi) - \int_{z=0}^{z=b \tan(\beta)} \frac{\gamma_s z}{b \tan(\beta)} dz \right) \sin\left(\frac{\pi}{4}\right) + s_u \cos\left(\frac{\pi}{4}\right) \right] \frac{\tan(\beta)}{\tan(\pi/4)} \quad (14)$$

Where the first two terms represent the horizontal component of the normal stress arising from soil strength and soil unit weight, respectively, and the last term represents the horizontal component of the shear stress. Equation (14) reduces to the following expression for  $H$ :

$$H = \left( \widehat{H}_p s_u - \frac{1}{2} \gamma_s b \tan^2(\beta) \right) b \quad (15)$$

$$\text{where } \widehat{H}_p = 3\pi \tan(\beta) \quad (16)$$

Calculations of  $\hat{H}_p$  determined using equation (16) are compared with corresponding FEA calculations in Table 5 for values of  $\alpha$  ranging between 0 and 1 and salient values of  $\beta$ . Very good agreement can be observed with a maximum deviation of 1.8%.

An empirical extension to equation (15) was again adopted to consider axisymmetric conditions where strong linearity was also evident in the  $\hat{H}_{axi}/\hat{H}_p - b/R_0^{0.7}$  relationship:

$$\hat{H}_{axi} = \hat{H}_p \left( 1 + n \left( \frac{b}{R_0} \right)^{0.7} \right) \quad (17)$$

$$n = 0.05 \tan(1.04\beta_{rad}) + 0.066 + 0.034\alpha \quad (18)$$

The resulting horizontal reaction can, therefore, be determined as follows:

$$H = \hat{H}_{axi} s_u A - \gamma_s \pi \tan^2 \beta \left[ b^2 R_0 + \frac{b^3}{3} \right] \quad (19)$$

Figure 18 compares calculations determined using equations (15) – (17) to the FEA output for both PS and axisymmetric conditions where strong agreement can be observed, albeit with a slight over-prediction for smaller caisson radii.

#### *Application: large-diameter caisson at Bridgewater, UK*

The proposed design methodology is retrospectively applied to a recent case history involving the construction of a 13 m external diameter reinforced concrete caisson at Bridgewater, UK (Royston 2018). Key caisson/soil parameters are presented in Table 6. Predictions of the total anchor anti-flotation resistance contribution (determined using equation (13)) and the developed horizontal reaction (determined using equation (19)) are plotted as a function of the anchor width in Figs. 19(a) and 19(b) respectively for key values of  $\alpha$  and  $\beta$ . Also shown in Fig. 19(a) is the net flotation force,  $F_{net}$ , determined from water and soil buoyancy minus the downward weight of the caisson walls:

$$F_{net} = \pi [\gamma_w R_0^2 (h - z_w) + \gamma'_s R_0^2 h - \gamma_c (R_0^2 - (R_0 - t)^2) h] \quad (20)$$

Where  $\gamma_w$  and  $\gamma_c$  are the unit weight of water and concrete respectively,  $\gamma'_s$  is the effective soil unit weight,  $h$  is the caisson embedded depth,  $z_w$  is the depth to the water table, and  $t$  is the thickness of the shaft wall. Equation (20) assumes an empty tank and zero external caisson-soil skin friction on account of the use of lubrication during the sinking stage as a worst-case scenario. For the Bridgewater caisson,  $F_{net}$  was determined as 16.6 MN; this equates to 664 m<sup>3</sup> of mass concrete if design option (c) is adopted (anti-flotation met with dead weight only). If design option (b) is instead adopted (anti-flotation met with an enlarged base only), it can be seen from Fig. 19(a) that  $b \approx 0.5$  m is required for a rough anchor with  $\beta = 75^\circ$ . This contrasts with a value of  $b \approx 0.55$  m for  $\beta = 0^\circ$  (regardless of  $\alpha$ ) and  $b \approx 0.7$  m for  $\beta = 75^\circ$  with a smooth interface.

Figure 19(b) shows that the choice of anchor geometry has a substantial influence on the developed horizontal reaction and, therefore, the structural design of the caisson walls. By way of example, values of  $\beta$  of  $0^\circ$ ,  $45^\circ$  and  $75^\circ$  induce horizontal reactions of 0 MN, 12.2 MN and 45.8 MN respectively for a  $b = 0.5$  m anchor regardless of the anchor roughness. These results underline that

efficient and economical use of an enlarged caisson base for anti-flotation resistance requires an integrated geotechnical and structural design approach.

## CONCLUSIONS

This paper has described a numerical investigation of the uplift capacity and resulting horizontal reaction for an under-reamed open caisson shaft with an enlarged base embedded in undrained soil. Two-dimensional numerical analysis was adopted for this purpose in conjunction with a custom adaptive remeshing strategy to reveal soil failure mechanisms. A parametric study explored the dependence of the uplift factor and horizontal reaction on the taper angle, interface roughness, soil unit weight, and caisson radius.

For plane strain conditions, failure was shown to correspond to a local ‘flow-around’ mechanism comprising a rigid triangular region immediately above the anchor, a shear fan zone and another rigid triangular region beneath the anchor. The resulting relationship between the uplift factor,  $N_p$ , and the taper angle,  $\beta$ , was shown to be strongly dependent on the interface roughness,  $\alpha$ . A reduction in  $\alpha$  caused (a) the range for which  $N_p$  is independent of  $\beta$  to be reduced, (b) the relationship between  $\beta$  and  $N_p$  to become linear and (c) a reduction in  $N_p$  for an increasing  $\beta$ .

Consideration of axisymmetric behaviour influenced the soil failure mechanism in three ways: (a) the shape of the shear fan zone transitioned from circular to spiral, (b) plastic work occurred in the previously rigid wedge and (c) the circumferential length of the failure surface reduced leading to an increase in the shear strain. These factors combined to produce notably greater uplift capacities where the relationship between the uplift factor and dimensionless caisson radius was both non-linear and highly dependent on the anchor taper angle. In contrast, while  $\alpha$  was also shown to have an effect, its influence was deemed secondary to both  $\beta$  and the dimensionless caisson radius.

The finite element results also showed that the use of a steep taper angle (high  $\beta$ ) has the potential to induce a large horizontal reaction and therefore significant compressive stresses in the walls at the base of the shaft. For plane strain conditions, the relationship between the normalised horizontal reaction and  $\beta$  was shown to be independent of  $\alpha$  since the horizontal reaction is dominated by the normal stress contribution of the soil strength and unit weight. However, the extension of the problem to axisymmetric behaviour introduced a slight sensitivity to  $\alpha$ .

The soil failure mechanisms obtained from the two-dimensional finite element analyses informed the development of simplified closed-form design equations suitable for use in routine design. This exercise involved the use of upper bound plasticity theory for plane strain conditions whereas empirical extensions, through curve-fitting the numerical output, were used to extend the design method to axisymmetric behaviour. In all cases, both FEA- and FELA-calculated failure loads and FEA-calculated horizontal reactions obtained were shown to be in excellent agreement with the developed simplified equations.



By way of example, the proposed design methodology was retrospectively applied to a recent case history involving the construction of a large diameter caisson at Bridgewater, UK. The results showed that while an enlarged caisson base is an effective means of achieving anti-flotation resistance, the choice of anchor geometry has a substantial influence on the developed horizontal reaction and therefore the structural design of the caisson walls. Efficient and economical use of an enlarged caisson base for anti-flotation resistance, therefore, requires an integrated geotechnical and structural design approach.

Finally, simplifying assumptions have necessarily been adopted to numerically model the caisson uplift problem. In particular, the present analyses and developed design methodology is limited to the deep failure condition and therefore deep caisson shafts. For shallow embedments, this assumption is likely to provide an over-estimate of the uplift capacity.

### Acknowledgements

This project was supported by the Royal Academy of Engineering under the Research Fellowship Scheme and the Engineering and Physical Sciences Research Council (grant no. EP/T006900/1). For the purpose of Open Access, the author has applied a CC BY public copyright licence to any Author Accepted Manuscript version arising from this submission.

### Notation list

$\alpha$	Anchor-soil interface roughness factor
$\beta$	Anchor taper angle
$\beta_{\text{rad}}$	Anchor taper angle defined explicitly in radians
$\gamma_c$	Unit weight of concrete
$\gamma_s$	Unit weight of the soil
$\gamma_w$	Unit weight of water
$\gamma'_s$	Effective unit weight of the soil
$\Delta E$	Energy dissipated by internal soil stresses
$\Delta W_p$	Work done by external forces
$\Delta W_s$	Work done by soil weight
$\theta_I, \theta_{II}, \theta_{III}$	Angles defining assumed soil failure mechanism
$\theta_T$	Lode angle governing the rounding of corners of the failure criterion
$\nu_u$	Undrained Poisson's ratio of the soil
$A$	Plan cross-sectional area of the anchor
$b$	Anchor width
$E_u$	Undrained Young's modulus of the soil
$F_{\text{net}}$	Net flotation force
$h$	Embedded depth of the shaft
$H$	Developed horizontal reaction on the shaft during uplift
$H_p$	Developed horizontal reaction on the shaft during uplift for plane strain conditions
$\hat{H}_{\text{axi}}$	Normalised horizontal reaction for axisymmetric conditions
$\hat{H}_p$	Normalised horizontal reaction for plane strain conditions
$k$	Increment of soil undrained shear strength with depth
$K_0$	Coefficient of lateral earth pressure at rest
$M$	Curve-fitting parameter

---

$N_{\text{axi}}$	Dimensionless uplift factor for axisymmetric conditions
$N_p$	Dimensionless uplift factor for plane strain conditions
$R_0$	External radius of the shaft
$s_u$	Soil undrained shear strength at the anchor apex
$s_u(z)$	Soil undrained shear strength at depth $z$
$t$	Thickness of the shaft wall
$u$	Uplift displacement of shaft
$V$	Shaft vertical uplift force
$V_{\text{axi}}$	Shaft vertical uplift resistance for axisymmetric conditions
$V_p$	Shaft vertical uplift resistance for plane strain conditions
$v_0$	Upward velocity of the shaft during uplift loading
$z$	Elevation relative to the anchor apex
$z_w$	Depth to the ground water table

## References

- Abbo, A.J., Lyamin, A.V., Sloan, S.W., Hambleton, J.P., 2011. A C2 continuous approximation to the Mohr–Coulomb yield surface. *Int. J. Solids Struct.* 48, 3001–3010.  
<https://doi.org/10.1016/j.ijsolstr.2011.06.021>
- Bhattacharya, P. and Kumar, J., 2014. Pullout capacity of inclined plate anchors embedded in sand. *Canadian Geotechnical Journal*, 51(11), pp.1365-1370.
- Das, B.M., 1978. Model tests for uplift capacity of foundations in clay. *Soils and Foundations*, 18(2), pp.17-24.
- Das, B.M., 1980. A procedure for estimation of ultimate uplift capacity of foundations in clay. *Soils and foundations*, 20(1), pp.77-82.
- Das, B.M., Tarquin, A.J. and Moreno, R., 1985a. Model tests for pullout resistance of vertical anchors in clay. *Civil engineering for practicing and design engineers*, 4(2), pp.191-209.
- Das, B.M., Moreno, R. and Dallo, K.F., 1985b. Ultimate pullout capacity of shallow vertical anchors in clay. *Soils and Foundations*, 25(2), pp.148-152.
- Das, B.M., Shin, E.C., Dass, R.N. and Omar, M.T., 1994. Suction force below plate anchors in soft clay. *Marine Georesources & Geotechnology*, 12(1), pp.71-81.
- Dassault Systèmes, 2017. Abaqus FEA.
- Jesmani, M., Kamalzare, M. and Nazari, M., 2013. Numerical study of behavior of anchor plates in clayey soils. *International Journal of Geomechanics*, 13(5), pp.502-513.
- Kumar, J. and Rahaman, O., 2018. Vertical uplift resistance of horizontal plate anchors for eccentric and inclined loads. *Canadian Geotechnical Journal*, 56(2), pp.290-299.
- Martin, C.M., 2011. The use of adaptive finite-element limit analysis to reveal slip-line fields. *Géotechnique Lett.* 1, 23–29. <https://doi.org/10.1680/geolett.11.00018>
- Merifield, R.S., Sloan, S.W. and Yu, H.S., 2001. Stability of plate anchors in undrained clay. *Geotechnique*, 51(2), pp.141-153.
- Merifield, R.S., Lyamin, A.V., Sloan, S.W. and Yu, H.S., 2003. Three-dimensional lower bound solutions for stability of plate anchors in clay. *Journal of Geotechnical and Geoenvironmental Engineering*, 129(3), pp.243-253.
- Merifield, R.S., Lyamin, A.V. and Sloan, S.W., 2005. Stability of inclined strip anchors in purely cohesive soil. *Journal of Geotechnical and Geoenvironmental Engineering*, 131(6), pp.792-799.

- Merifield, R.S. and Sloan, S.W., 2006. The ultimate pullout capacity of anchors in frictional soils. *Canadian Geotechnical Journal*, 43(8), pp.852-868.
- O'Neill, M.P., Bransby, M.F. and Randolph, M.F., 2003. Drag anchor fluke soil interaction in clays. *Canadian Geotechnical Journal*, 40(1), pp.78-94.
- Phillips, B.M., Royston, R., Sheil, B.B. & Byrne, B.W. (2019). "Instrumentation and monitoring of a concrete jacking pipe." *International Conference on Smart Infrastructure and Construction (ICSIC)*, Cambridge, UK. Institution of Civil Engineers, London, UK (MJ DeJong, JM Schooling and GMB Viggiani). DOI: 10.1680/icsic.64669.457.
- Rowe, R.K. and Davis, E.H., 1982. The behaviour of anchor plates in clay. *Geotechnique*, 32(1), pp.9-23.
- Roy, A. and Bhattacharya, P., 2018. Diameter effect on uplift capacity of horizontal circular anchor embedded in sand. *International Journal of Geotechnical Engineering*, pp.1-14.
- Royston, R. 2018. Investigation of soil-structure interaction for large diameter caissons. DPhil thesis. University of Oxford.
- Royston, R., Sheil, B.B. and Byrne, B.W. 2016 Bearing capacity beneath tapered blades of open dug caissons in sand. *Civil Engineering Research in Ireland, Galway, Ireland*.
- Royston, R., Sheil, B.B. & Byrne, B.W. (2020a) Monitoring the construction of a large-diameter caisson in sand. *Proceedings of the ICE - Geotechnical Engineering*. DOI: 10.1680/jgeen.19.00266.
- Royston, R., Sheil, B.B. & Byrne, B.W. (2020b) Undrained bearing capacity of the cutting face of large-diameter caissons. *Géotechnique*. DOI: 10.1680/jgeot.20.P.210.
- Sheil, B.B., 2021. Hybrid framework for forecasting circular excavation collapse: Combining physics-based and data-driven modeling. *Journal of Geotechnical and Geoenvironmental Engineering*, 147(12), p.04021140. DOI: 10.1061/(ASCE)GT.1943-5606.0002683.
- Sheil, B. & Templeman, J. (2022). Bearing capacity of large-diameter open caissons embedded in sand. *Géotechnique*. Published online ahead of print. DOI: 10.1680/jgeot.21.00089.
- Shewchuk, J.R., 2002. Delaunay refinement algorithms for triangular mesh generation. *Comput. Geom.* 22, 21–74. [https://doi.org/10.1016/S0925-7721\(01\)00047-5](https://doi.org/10.1016/S0925-7721(01)00047-5)
- Shewchuk, J.R., 1996. Triangle: Engineering a 2D quality mesh generator and Delaunay triangulator, in: *Applied Computational Geometry: Towards Geometric Engineering*, Lecture Notes in Computer Science. Presented at the Workshop on Applied Computational Geometry, pp. 203–222. <https://doi.org/10.1007/BFb0014497>.
- Sloan, S.W., Abbo, A.J., Sheng, D., 2001. Refined explicit integration of elastoplastic models with automatic error control. *Eng. Comput.* 18, 121–154. <https://doi.org/10.1108/02644400110365842>
- Song, Z., Hu, Y. and Randolph, M.F., 2008. Numerical simulation of vertical pullout of plate anchors in clay. *Journal of geotechnical and geoenvironmental engineering*, 134(6), pp.866-875.
- Templeman, J.O., Phillips, B.M. & Sheil, B.B. (2021) Cutting shoe design for open caissons in sand: influence on vertical bearing capacity. *Proceedings of the ICE - Geotechnical Engineering*. Published online ahead of print.
- Thorne, C.P., Wang, C.X. and Carter, J.P., 2004. Uplift capacity of rapidly loaded strip anchors in uniform strength clay. *Geotechnique*.
- Vesic, A. S. 1971. Breakout resistance of objects embedded in ocean bottom. *Journal of the Soil Mechanics and Foundations Division*, 97(9), 1183–1205.

Wang, D., Hu, Y. and Randolph, M.F., 2010. Three-dimensional large deformation finite-element analysis of plate anchors in uniform clay. *Journal of geotechnical and geoenvironmental engineering*, 136(2), pp.355-365.

Yu, S.B., Hambleton, J.P. and Sloan, S.W., 2015. Undrained uplift capacity of deeply embedded strip anchors in non-uniform soil. *Computers and Geotechnics*, 70, pp.41-49.

Zhao, X., Randolph, M. F., Wang, D., & Gaudin, C. (2015). Upper bound analysis of uplift capacity of a tapered plate anchor in cohesive soil. *Géotechnique Letters*, 5(3), 205-211.

Table 1 Validation of finite element model through comparisons to FELA and previous solutions

Reference	Analysis	Uplift factor, $N_p$
Present study	FEA	Smooth: 11.459 Rough: 11.457
Present study	FELA	Smooth: 11.46 (UB), 11.33 (LB) Rough: 11.45 (UB), 11.35 (LB)
Merifield et al. (2001)	Finite element limit analysis	11.16 (LB), 11.86 (UB)*
O'Neill et al. (2003)	FEA	11.87

\*These values are “applicable to both rough and smooth anchors”

Table 2 Calculation of energy dissipation by internal stresses: mechanism I.

Discontinuity/ region	Length	Velocity jump ( $\Delta v$ ) or velocity ( $v$ )	Energy dissipated
AC	$\frac{b}{\cos\left(\frac{\pi}{4}\right)}$	$v_0 \sin\left(\frac{\pi}{4}\right)$	$s_u v_0 b$
CD	$\frac{b}{\cos\left(\frac{\pi}{4}\right)} \theta_{II}$	$v_0 \cos\left(\frac{\pi}{4}\right)$	$s_u v_0 b \frac{3\pi}{2}$
DE	$\frac{b}{\cos\left(\frac{\pi}{4}\right)}$	$v_0 \cos\left(\frac{\pi}{4}\right)$	$s_u v_0 b$
ACDA	-	$v_0 \cos\left(\frac{\pi}{4}\right)$	$s_u v_0 b \frac{3\pi}{2}$

Table 3 Calculation of energy dissipation by internal stresses: mechanism II.

Discontinuity/ region	Length	Velocity jump ( $\Delta v$ ) or velocity ( $v$ )	Energy dissipated
AB	$\frac{b}{\cos(\beta)}$	$\frac{v_0 \sin(\beta_{\text{rad}} + \theta_I)}{\sin\left(\frac{\pi}{2} + \theta_I\right)}$	$\alpha s_u \frac{b}{\cos(\beta)} \frac{v_0 \sin(\beta_{\text{rad}} + \theta_I)}{\sin\left(\frac{\pi}{2} + \theta_I\right)}$
BC	$\frac{b}{\cos(\beta)} \sin(\theta_I)$	$\frac{v_0 \sin\left(\frac{\pi}{2} - \beta_{\text{rad}}\right)}{\sin\left(\frac{\pi}{2} + \theta_I\right)}$	$s_u \frac{b}{\cos(\beta)} \sin(\theta_I) \frac{v_0 \sin\left(\frac{\pi}{2} - \beta_{\text{rad}}\right)}{\sin\left(\frac{\pi}{2} + \theta_I\right)}$
CD	$\frac{b}{\cos(\beta)} \cos(\theta_I) \left(\frac{7\pi}{4} - \beta_{\text{rad}} - \theta_I\right)$	$\frac{v_0 \sin\left(\frac{\pi}{2} - \beta_{\text{rad}}\right)}{\sin\left(\frac{\pi}{2} + \theta_I\right)}$	$s_u \frac{b}{\cos(\beta)} \cos(\theta_I) \left(\frac{7\pi}{4} - \beta_{\text{rad}} - \theta_I\right) \frac{v_0 \sin\left(\frac{\pi}{2} - \beta_{\text{rad}}\right)}{\sin\left(\frac{\pi}{2} + \theta_I\right)}$
DE	$\frac{b}{\cos(\beta)} \cos(\theta_I)$	$\frac{v_0 \sin\left(\frac{\pi}{2} - \beta_{\text{rad}}\right)}{\sin\left(\frac{\pi}{2} + \theta_I\right)}$	$s_u \frac{b}{\cos(\beta)} \cos(\theta_I) \frac{v_0 \sin\left(\frac{\pi}{2} - \beta_{\text{rad}}\right)}{\sin\left(\frac{\pi}{2} + \theta_I\right)}$
ACDA	-	$\frac{v_0 \sin\left(\frac{\pi}{2} - \beta_{\text{rad}}\right)}{\sin\left(\frac{\pi}{2} + \theta_I\right)}$	$s_u \frac{b}{\cos(\beta)} \cos(\theta_I) \left(\frac{7\pi}{4} - \beta_{\text{rad}} - \theta_I\right) \frac{v_0 \sin\left(\frac{\pi}{2} - \beta_{\text{rad}}\right)}{\sin\left(\frac{\pi}{2} + \theta_I\right)}$

Table 4 Dimensionless uplift factors,  $N_p$ , for different values of the roughness factor and taper angle determined using all three methods considered in this study;  $\gamma_s b/s_u = 0$ .

	$\beta = 0^\circ$				$\beta = 30^\circ$				$\beta = 45^\circ$				$\beta = 60^\circ$			
$\alpha$	M <sub>a</sub>	UB	FE A	FEL A <sup>b</sup>	M <sub>a</sub>	UB	FE A	FEL A <sup>b</sup>	M <sub>a</sub>	UB	FE A	FEL A <sup>b</sup>	M <sub>a</sub>	UB	FE A	FEL A <sup>b</sup>
0	I	11. 42	11. 46	11.4 1	II	10. 38	10. 40	10.3 6	II	9.8 5	9.8 8	9.83	II	9.3 3	9.3 9	9.31
0. 25	I	11. 42	11. 45	11.4 1	II	10. 74	10. 77	10.7 3	II	10. 33	10. 35	10.3 0	II	9.9 9	10. 02	9.96
0. 5	I	11. 42	11. 46	11.4 1	II	11. 05	11. 09	11.0 2	II	10. 74	10. 77	10.7 2	II	10. 59	10. 61	10.5 6
0. 75	I	11. 42	11. 46	11.4 1	II	11. 32	11. 34	11.3 0	II	11. 11	11. 13	11.0 9	II	11. 14	11. 16	11.1 2
1. 0	I	11. 42	11. 46	11.4 1	I	11. 42	11. 44	11.4 0	II	11. 42	11. 45	11.4 0	II	11. 63	11. 69	11.6 1

<sup>a</sup>M = mechanism type (see Fig. 15). <sup>b</sup>FELA results present the average of the UB and LB values

Table 5 Dimensionless horizontal reactions,  $\hat{H}_p$ , for different values of the roughness factor and taper angle determined using equation (15) and FEA;  $\gamma_s b/s_u = 0$ .

	$\beta = 30^\circ$		$\beta = 45^\circ$		$\beta = 60^\circ$	
$\alpha$	Eq. (16)	FEA	Eq. (16)	FEA	Eq. (16)	FEA
0	5.99	6.01	9.86	9.88	16.16	16.26
0.25	5.87	5.89	9.82	9.85	16.29	16.35
0.5	5.72	5.74	9.74	9.77	16.34	16.39
0.75	5.54	5.56	9.61	9.64	16.29	16.34
1.0	5.44	5.34	9.42	9.43	16.15	16.16

Table 6 Caisson/soil parameters reported by Royston (2018) used for example application of the proposed design methodology.

Parameter	Value
Caisson internal radius, $R_0$ (m)	6.5
Caisson wall thickness, $t$ (m)	1
Caisson formation depth, $h$ (m)	20
Soil undrained shear strength, $s_u$ (kPa)	60
Total soil unit weight, $\gamma_s$ (kN/m <sup>3</sup> )	16
Concrete caisson wall weight, $\gamma_c$ (kN/m <sup>3</sup> )	25
Depth below ground level to water table, $z_w$ (m)	5

### Figure captions

Figure 1 Large diameter caisson shaft under construction by Ward and Burke Construction Ltd for an underground pumping station at Blackpool, UK.

Figure 2 Problem definition showing typical caisson shaft features and the key parameters explored in this numerical study.

Figure 3 Octahedral section of the adopted yield criterion showing the rounding of the edge discontinuities compared to the conventional Tresca surface in the deviatoric plane.

Figure 4 Overview of the adaptive remeshing FEA procedure.

Figure 5 Exemplar FEA mesh for a deep plane strain horizontal plate anchor: (a) initial coarse mesh and (b) mesh after five rounds of adaptive mesh refinement based on maximum shear strain rates.  $\beta = 0^\circ$ ,  $\alpha = 0$ ,  $\gamma_s b/s_u = 0$ , PS,  $kb/s_u = 0$ .

Figure 6 Contours of total soil displacement magnitudes at failure superimposed on the refined meshes for a tapered anchor loaded vertically upwards for different values of  $\alpha$  and  $\beta$ ; PS,  $\gamma_s b/s_u = 0$ ,  $kb/s_u = 0$ . Note each colour contour was scaled between the maximum (red) and minimum (blue) displacement in the respective subplot.

Figure 7 FEA calculations of the influence of  $\beta$  on the anchor uplift factor for (a) values of  $\alpha$  ranging between 0 and 1 with  $\gamma_s b/s_u = 0$ ; and (b) a variation in  $\gamma_s b/s_u$  for both a rough and smooth anchor; PS,  $kb/s_u = 0$ .

Figure 8 Contours of total soil displacement magnitudes at failure superimposed on the refined meshes for a tapered anchor considering the influence of both  $\beta$  and  $b/R_0$ ;  $\alpha = 1$ ,  $\gamma_s b/s_u = 0$ ,  $kb/s_u = 0$ . Note each colour contour was scaled between the maximum (red) and minimum (blue) displacement in the respective subplot.

Figure 9 FEA calculations of the influence of dimensionless caisson radius on the relative anchor uplift capacity for a (a) smooth and (b) rough interface;  $\gamma_s b/s_u = 0$ ,  $kb/s_u = 0$ .

Figure 10 FEA calculations of the influence of the gradient of  $s_u$  with depth on the anchor uplift factor for a (a) plane strain ( $b/R_0 = 0$ ) and (b) axisymmetric ( $b/R_0 = 0.3$ ) caisson;  $\gamma_s b/s_u = 0$ .

- Figure 11 LDFEA calculations considering linear (L) and non-linear (NL) geometric effects of the influence of soil stiffness on the anchor uplift factor for a typical plane strain caisson;  $\beta = 45^\circ$ ,  $\alpha = 1.0$ ,  $\gamma_s b/s_u = 0$ ,  $kb/s_u = 0$ .
- Figure 12 FEA calculations of the influence of  $\beta$  on the developed normalised horizontal reaction for values of  $\alpha$  ranging between 0 and 1 and for values of  $\gamma_s b/s_u$  of 0 and 1; PS.
- Figure 13 FEA calculations of the influence of  $b/R_0$  on the relative normalised horizontal reaction for a smooth and rough interface;  $\gamma_s b/s_u = 0$ .
- Figure 14 LDFEA calculations considering linear (L) and non-linear (NL) geometric effects of the influence of soil stiffness on the developed normalised horizontal reaction for a typical plane strain caisson;  $\beta = 45^\circ$ ,  $\alpha = 1.0$ ,  $\gamma_s b/s_u = 0$ ,  $kb/s_u = 0$ .
- Figure 15 Upper bound failure mechanisms considered for this study: (a) mechanism I, (b) mechanism II.
- Figure 16 Comparison of incremental shear strains determined using FEA and optimum upper bound mechanisms for  $\beta = 45^\circ$  and values of  $\alpha$  of (a) 0, (b) 0.5 and (c) 1; PS,  $\gamma_s b/s_u = 0$ .
- Figure 17 Verification of design method for the uplift capacity through comparisons between equation (11) and numerical calculations.
- Figure 18 Verification of design method for the dimensionless horizontal reaction through comparisons between equation (17) and FEA calculations.
- Figure 19 Predictions of (a) anchor uplift resistance contribution and (b) developed horizontal reaction for the Bridgewater caisson (see Table 6 for parameters).



Figure 1



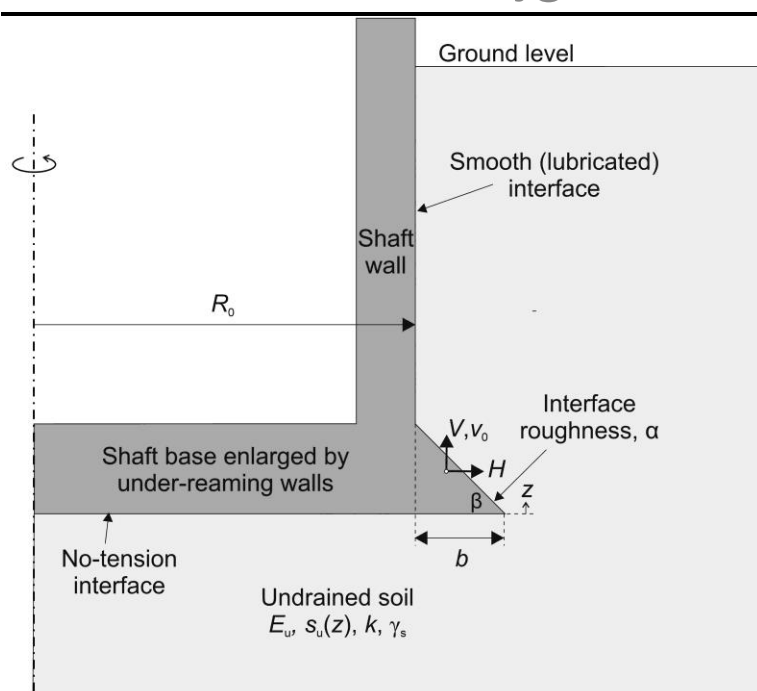


Figure 2

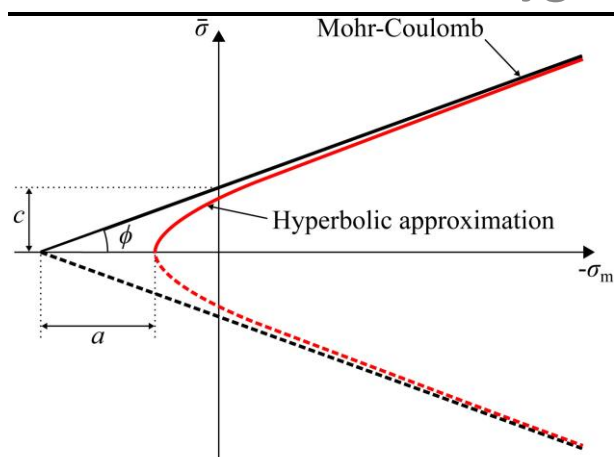


Figure 3

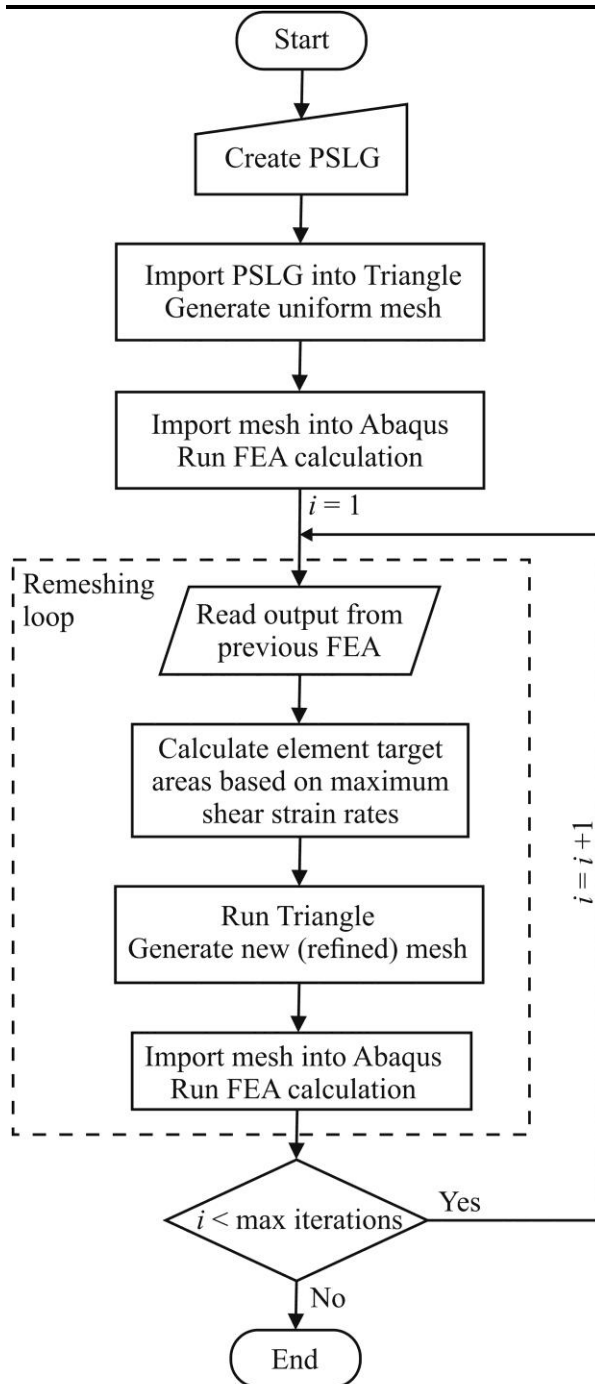


Figure 4

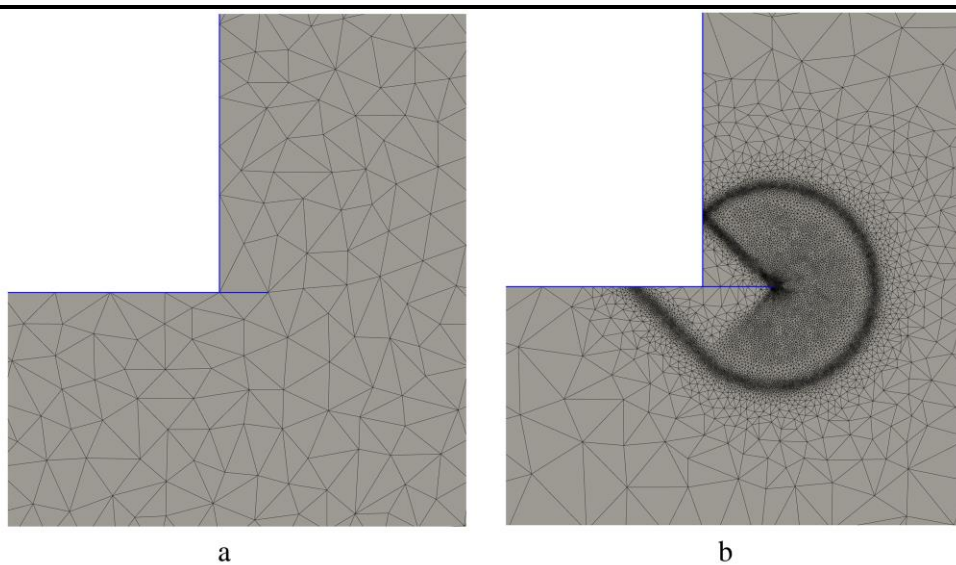


Figure 5

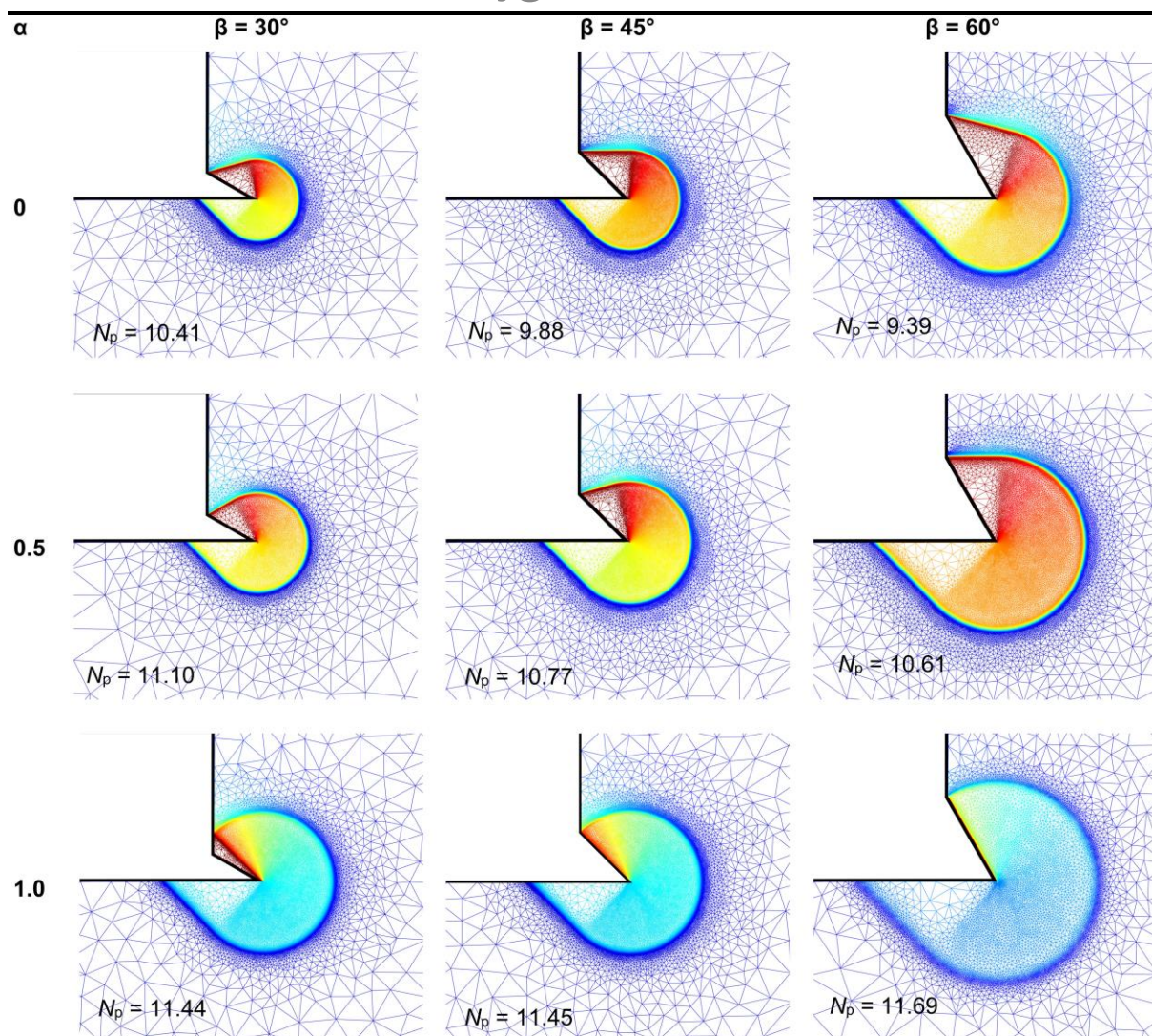


Figure 6

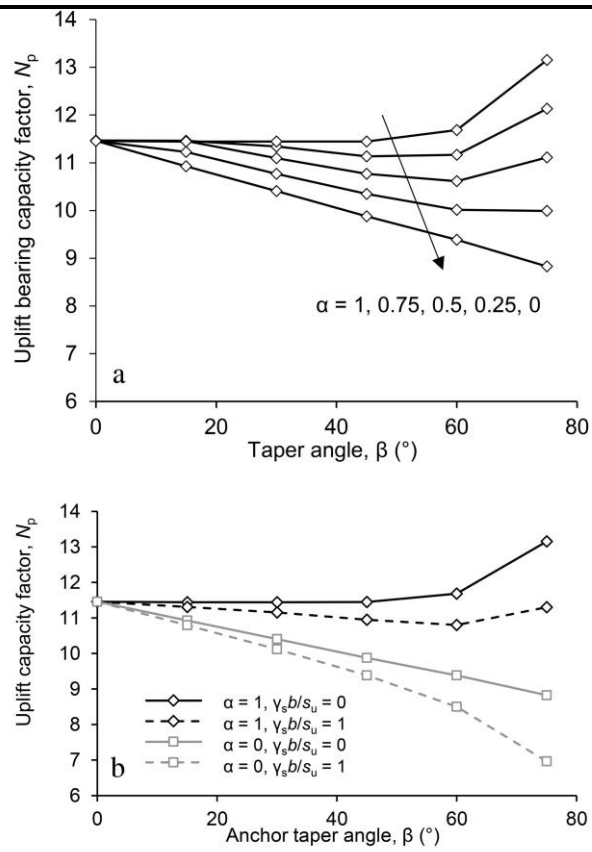


Figure 7



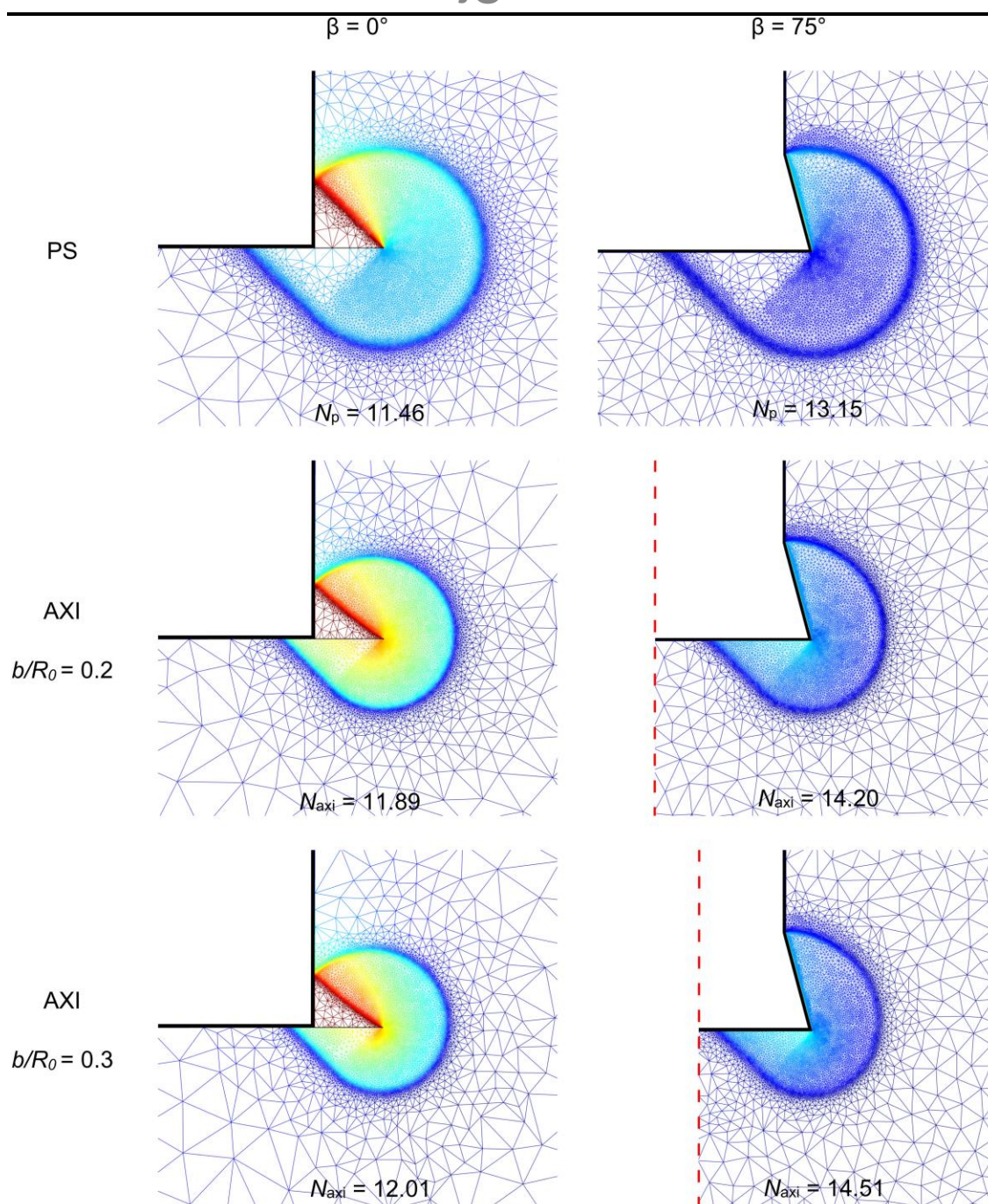


Figure 8

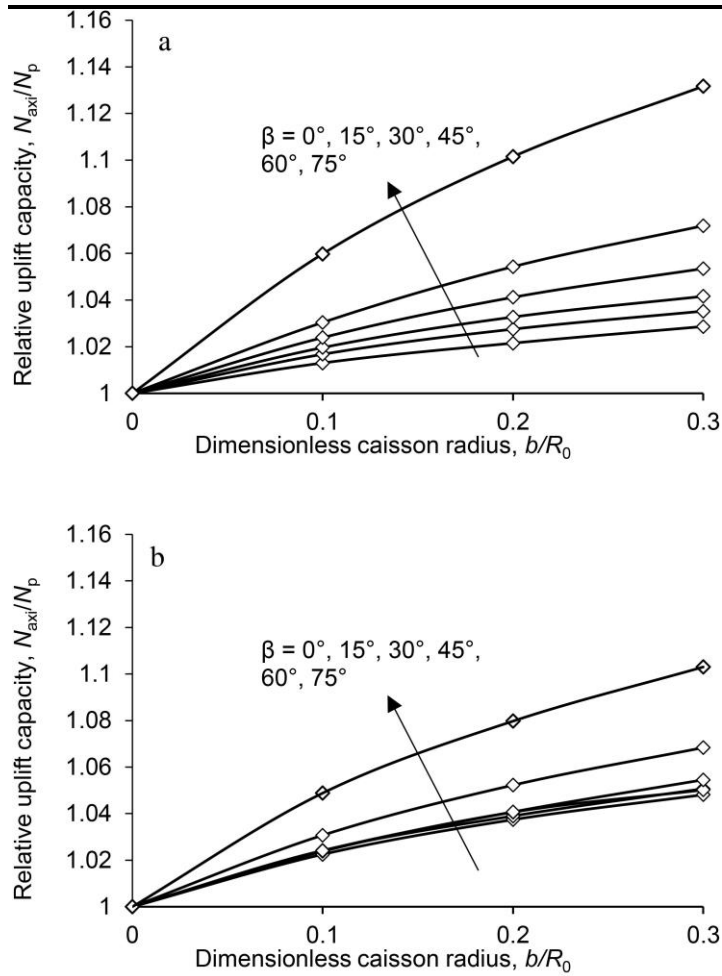


Figure 9



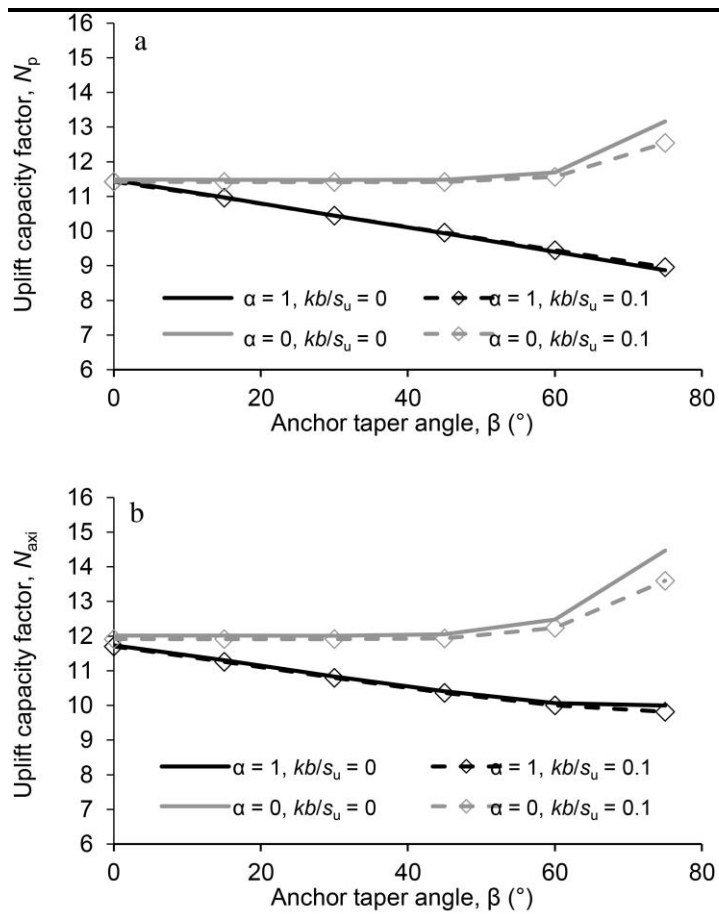


Figure 10

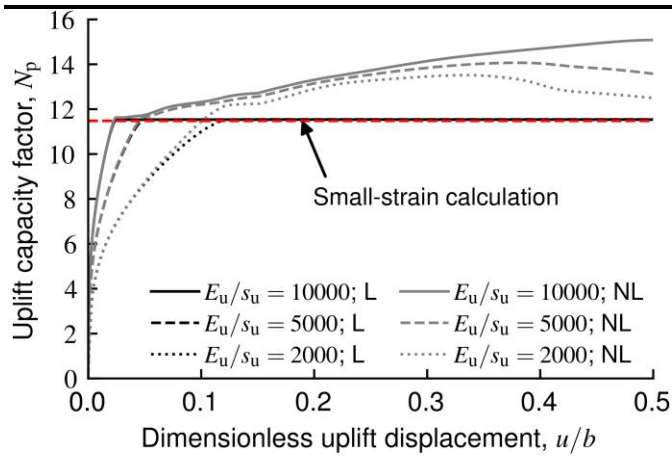


Figure 11

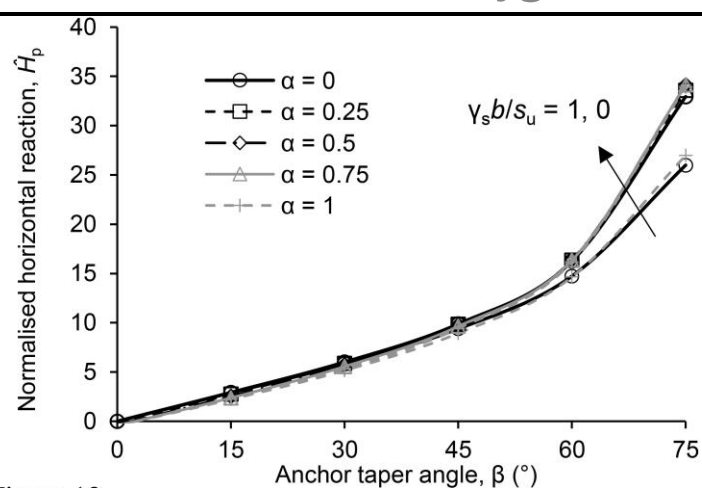


Figure 12

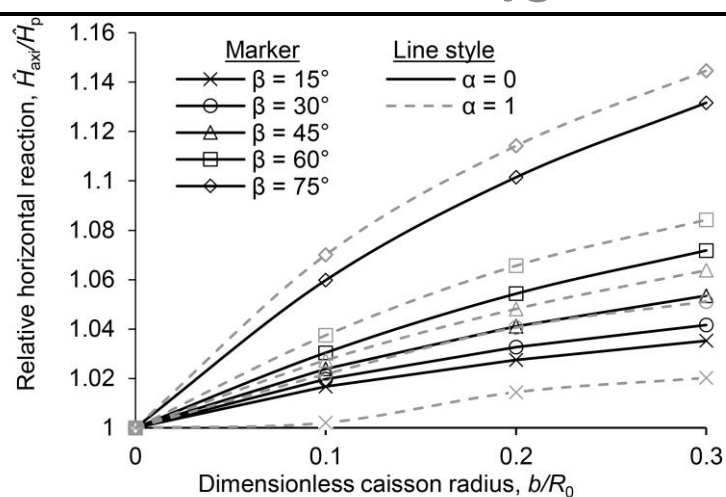


Figure 13

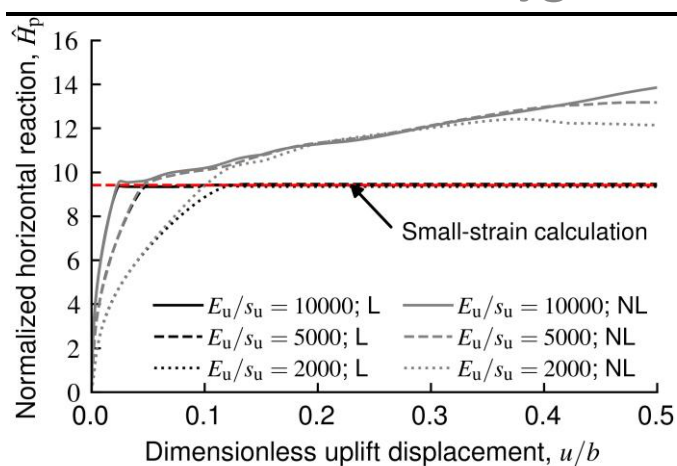


Figure 14

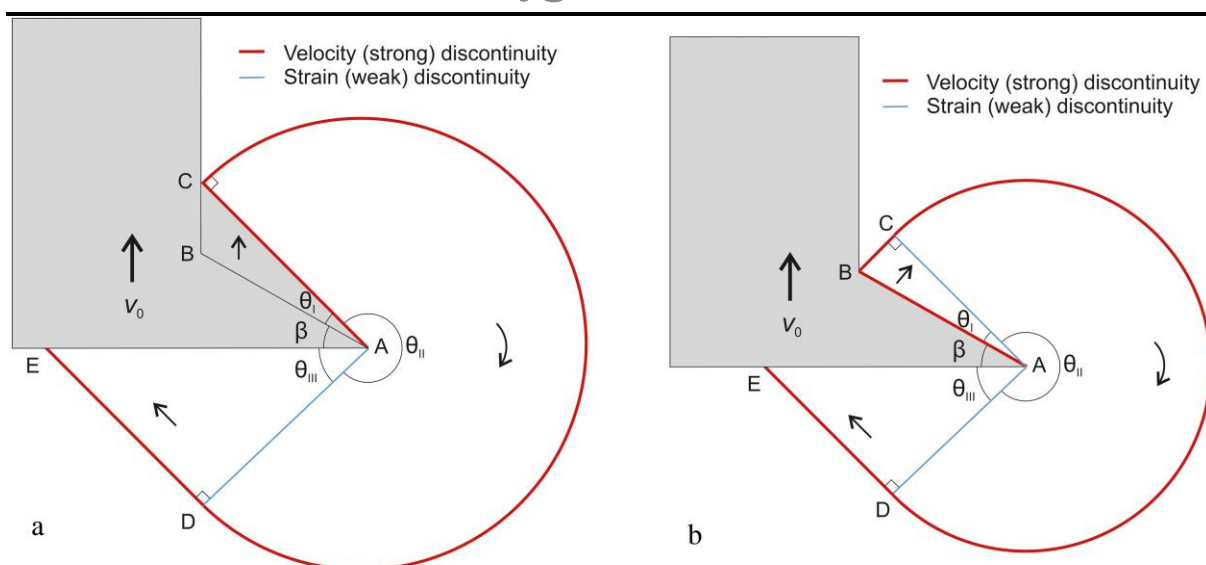
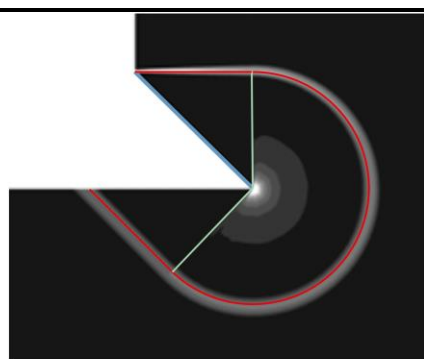
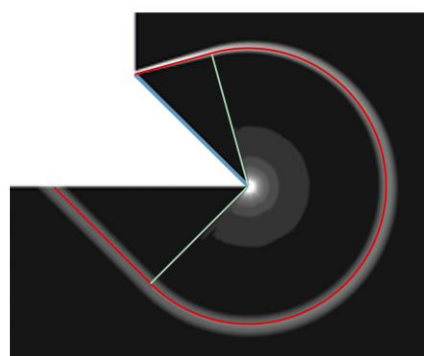


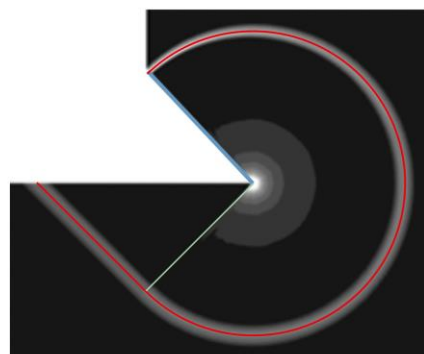
Figure 15



a



b



c

Figure 16

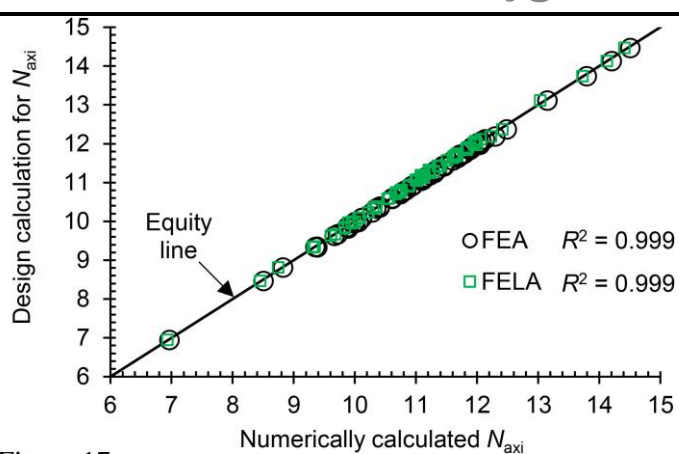


Figure 17



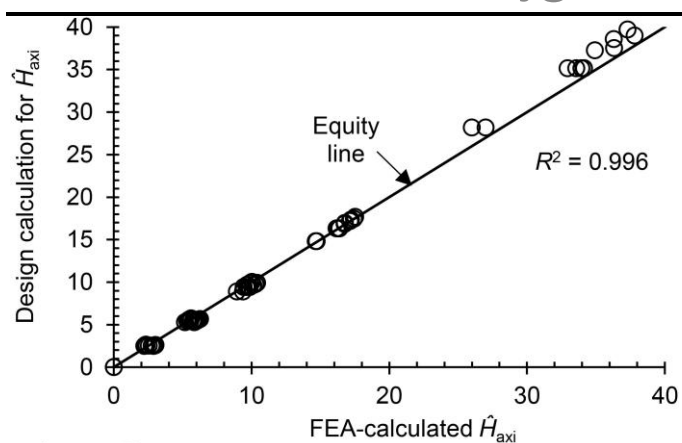


Figure 18

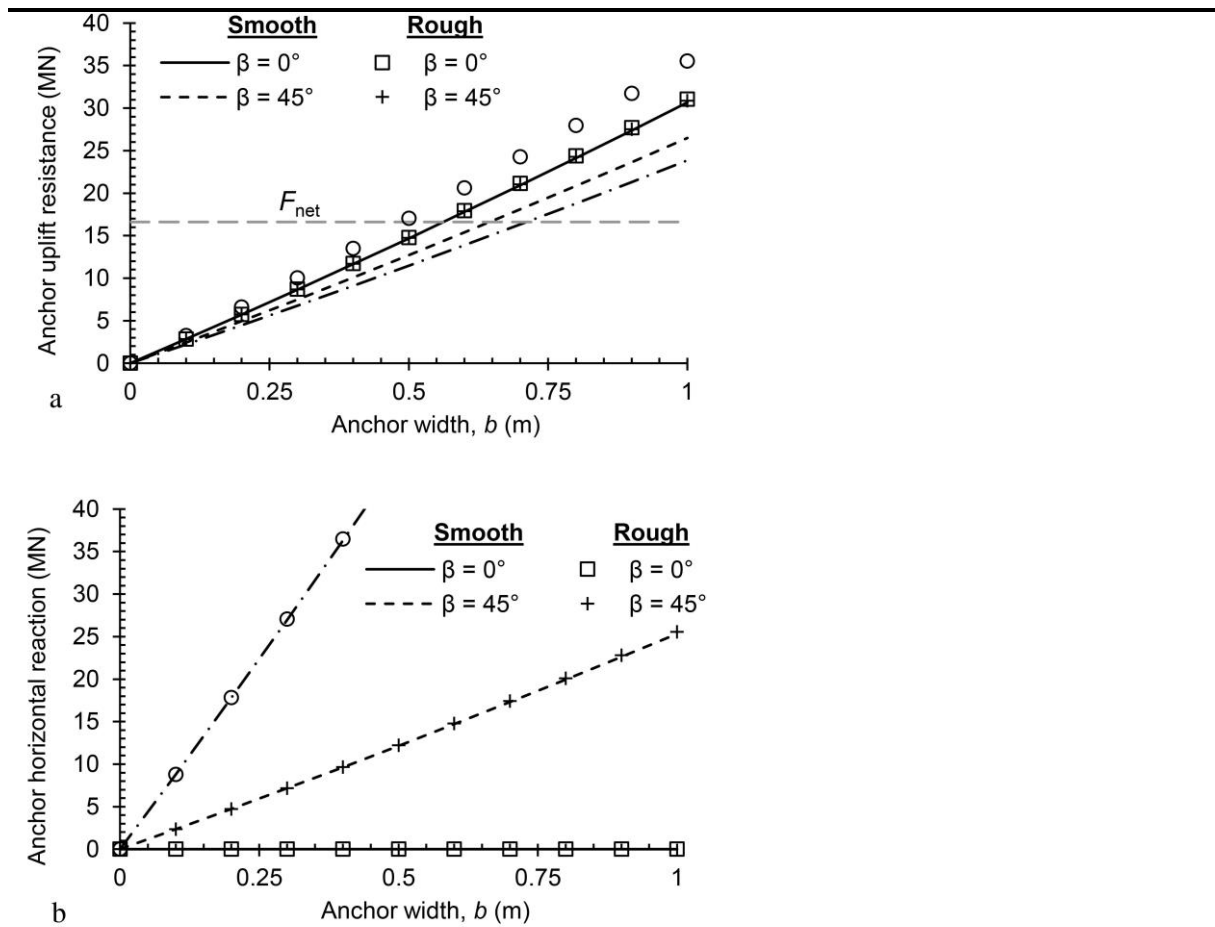


Figure 19